Real-Time Dynamic Atomic Spectroscopy Using Electro-Optic Frequency Combs

Nicolas Bourbeau Hébert,[1,2] Vincent Michaud-Belleau,[1,2] Christopher Perrella,[2] Gar-Wing Truong,[3,2]
James D. Anstie,[2] Thomas M. Stace,[4] Jérôme Genest,[1,2] and Andre N. Luiten[2*]

[1]*Centre d'Optique, Photonique et Laser, Université Laval, Québec, Québec G1V 0A6, Canada*
[2]*Institute for Photonics and Advanced Sensing (IPAS), School of Physical Sciences,
The University of Adelaide, Adelaide, South Australia 5005, Australia*
[3]*National Institute of Standards and Technology, Boulder, Colorado 80305, USA*
[4]*ARC Centre for Engineered Quantum Systems, University of Queensland,
Brisbane, Queensland 4072, Australia*
(Received 14 July 2016; published 25 October 2016)

Spectroscopy is a key technology for both fundamental and applied science. A long-held desire has been the development of a means to continuously acquire broadband spectral data with simultaneous high time and frequency resolution. Frequency-comb technology can open this door: here, we use a spectroscopic technique based on an electro-optic comb to make continuous observations of cesium vapor across a 3.2-GHz spectral bandwidth with a 2-μs time resolution and with 10-MHz frequency sampling. We use a rapidly switched pump laser to burn narrow features into the spectral line and study the response to this step perturbation. This examination allows us to see a number of unexpected effects, including the temporal evolution of the bandwidth, the amplitude, and the frequency of these burnt features. We also report on the previously unobserved effect of radiation reabsorption, which slowly produces a broad pedestal of perturbation around each feature. We present models that can explain these dynamical effects.

I. INTRODUCTION

Spectroscopy has long played a dual role in science: as a means to discover new and unpredicted behaviors as well as a stringent test bed for verifying theoretical predictions. Outside science, spectroscopy is a key industrial technology for the detection of trace materials and as a monitor of combustion, pollution, and chemical processes. The measurement of optical-transition frequencies has proved to be a powerful test for theoretical physics and finds practical application in assaying materials [1–3]. The advent of optical frequency combs has made the accurate determination of these transition frequencies almost routine. More information can be gained if one measures the line shape of an absorption or fluorescent process, rather than just its central frequency. In dilute vapors, this measurement can be used to elucidate state lifetimes, integrated number density [4], gas temperature [5–8], and transition probabilities between energy levels [9]. For high-density vapors, or in liquids and solids, the line shape can provide information on, e.g., vapor pressure [10,11], phonon spectra [12,13], molecular interactions [14,15], and collisional processes [16].

A wealth of new information could be gained with high-speed quantitative measurements of the line shape during a dynamical process driven by a chemical, optical, or physical change. This frontier is still relatively unexplored

experimentally: early examples of time-resolved observations can be seen in rapidly swept Fourier-transform infrared spectroscopy [17,18] or cavity-ringdown spectroscopy [19,20]. Here, the time resolution is usually limited to the millisecond-to-second time scale. For a higher time resolution, a stroboscopic-sampling approach can be used [21,22], although, naturally, these data are not continuous and the technique is only usable when the processes can be reproducibly triggered externally. Alternatively, time-resolved broad spectra can be obtained with the use of a swept-laser source. Tunable lasers can reach speeds on the order of 1–100 THz/s [23–25], with speeds exceeding 1000 THz/s just within reach [26]. Yet, high-speed tunable-laser spectroscopy faces two intrinsic challenges. First, unless a coherent approach is used, rapid tuning of the laser can distort narrow spectral features [27]. Second, the linear chirp limits the probe power before nonlinear effects are triggered. In fragile samples, such as those used in atomic spectroscopy or biological samples, the system being tested imposes a maximum instantaneous power (and thus a maximum SNR for a given acquisition time) to avoid saturation and damage. This constraint can be severe in realistic circumstances.

Frequency-comb techniques [13,28,29] can circumvent many of these problems by effectively observing the sample continuously at a large number of spectral points. Comb techniques have a theoretical limit of $\Delta t \Delta f \geq 1$ for a given time resolution Δt and frequency-sampling resolution Δf. However, many experiments

require broadband spectral coverage that greatly exceeds the detection bandwidth; this requirement necessarily results in an outcome that is far from the theoretical limit. For example, VIPA spectrometers spatially resolve comb spectra but can only reach resolutions on the order of the millisecond limited by the relatively low frame rate of most imagers [30–32]. Broad spectral coverage [33,34] can also be gained with dual-comb spectroscopy [35–38], but it suffers from a penalty because the intrinsic spectral compression leads to a product $\Delta t \Delta f$ that is necessarily worse by the number of comb modes [39].

In this article, we report the real-time, simultaneous observation of 320 spectral channels covering two optical transitions from the cesium (Cs) ground-state manifold with a microsecond time resolution and an approximately 10-MHz spectral sampling. We use an auxiliary laser that pumps the same manifold and observe rapid changes induced in the spectrum by making use of a recently demonstrated technique [40], based on a comb generated by the modulation of a continuous-wave (cw) laser [41–44]. The comb is directly mapped to the electrical domain without any spectral compression [40,45] in order to approach the ultimate Fourier limit. A tunable laser would need to scan at 3000 THz/s in order to make an equivalent measurement using a scanned approach. In order to aid the reader, we first summarize the salient elements of the apparatus, although we refer the reader to Ref. [40] for full details. We then describe our new findings on the evolution of multiple narrow-band features during optical pumping and relaxation back to equilibrium. We observe the real-time evolution of processes that are rather surprising: (a) an evolution of the amplitude, the frequency, and the bandwidth of the spectrally burnt features during the pumping process, and (b) the previously unobserved influence of radiation reabsorption on the transmission spectrum. We create models of the atomic-level dynamics and show good agreement with these new observations.

II. METHODS

Figure 1(a) shows the apparatus for the experiment. It is based on a comblike probe generated from a single Ti:sapphire cw laser tuned near 895 nm. Light from the laser, emitting at the frequency ν_c, is split into two paths: a fraction of the power is sent to an electro-optic modulator to generate a frequency comb by pseudorandom phase modulation [40]. A $2^9 - 1 = 511$ maximal length sequence is generated at 5 Gbits/s and delivered to the modulator to generate a comb with modes at frequencies of $\nu_c \pm n f_r$, where $f_r = 5$ GHz$/511 = 9.784\,74$ MHz is the repetition rate of the digital code. The resulting comb has a sinc²-shaped envelope, with its first zeros at ± 5 GHz. Here, the relative amplitude of the component at ν_c to that of neighboring modes is approximately 10 since the signal driving the modulator is not perfectly matched to its half-wave voltage. This stronger component does not affect the
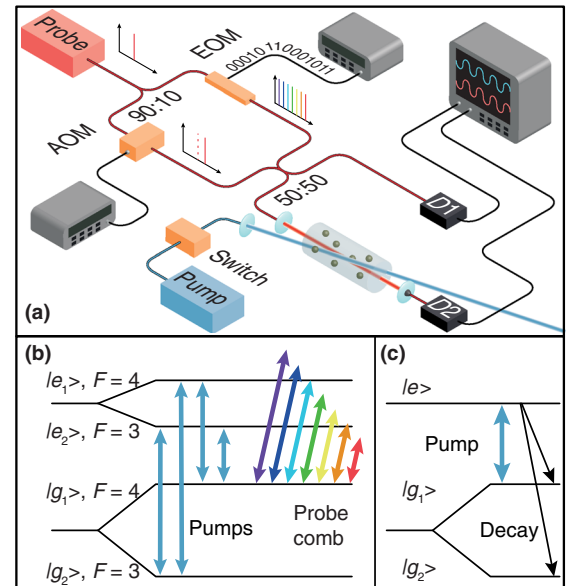

FIG. 1. (a) Experimental setup. The probe laser is split into two signals—one path is modulated with a pseudorandom number code to produce a user-controllable frequency comb, while the second is frequency shifted by an AOM to provide a local oscillator. The combined optical signals are then incident on a vapor cell. We separately detect the incident (D1) and transmitted (D2) light in two channels of a fast oscilloscope and then calculate the transmittance. (b) Cesium energy-level diagram showing the four possible arrangements for optical pumping between the two ground states and the two excited states, together with the transitions probed by the frequency comb. (c) Simplified three-level diagram which aids the calculation of the expected temporal response.

dynamic range of the instrument as long as it is shot-noise limited and the local oscillator (LO) is much stronger than the total comb power [46].

The advantage of electronically generated combs, when compared with combs generated by mode-locked lasers or microresonators, is the ability to optimize the comb characteristics to match the needs of the experiment. We have exploited this flexibility to generate a comb that efficiently translates the cw laser power into a comb that matches the spectral width of the cesium $D1$ manifold (the figures below only show a subset of the sampled data, focusing on the transitions), while also delivering a selectable high-density spectral sampling. The total averaged comb power incident on the atoms is approximately 100 μW, which corresponds to around 0.2 μW per mode near ν_c.

The remaining power from the cw laser is sent to an acousto-optic modulator (AOM) to generate a frequency-shifted signal to be used as a heterodyning LO for the comb. The comb and LO signals are combined in a 50∶50 coupler: one output is used as the input reference spectrum, while the second is sent through a 75-mm-long cesium vapor cell at a temperature of 22.2 °C, corresponding to a

vapor pressure of approximately 1 μTorr [47]. The frequency of the LO ($\nu_c + f_{\rm AOM}$) is chosen so that the mixing product from each comb mode sits at a unique frequency. We independently detect the reference and sample transmittance on two fast photodiodes and acquire their output simultaneously on the two channels of an 8-GHz oscilloscope operating at 20 GS/s. The experimental setup delivers both the amplitude and the phase through the cell, although, in this paper, we focus only on the transmittance. More details together with the calibration procedure are described in Ref. [40].

An auxiliary pump-laser beam (2.2 mm diameter, 200 μW $\sim 2I_{\rm sat}$) propagates through the vapor cell, and it crosses the probe beam (2.2 mm diameter) with an approximately 2° angle in the middle of the cell. The pump beam is switched on at $t = 0$ with a rise time of about 250 ns, held at constant power for 250 μs, and then switched off in approximately 250 ns. That pumping sequence runs continuously independently from the probe comb. An AOM is used as a fast optical switch because of its excellent extinction ratio. In this article, we demonstrate the influence of the pump in four separate arrangements where it connects either of the Cs ground states ($6S_{1/2}, F = 3$ or 4) to either of the exited states ($6P_{1/2}, F' = 3$ or 4), as shown on Fig. 1(b). Figure 1(c) shows a simplified three-level diagram that is used to model the expected temporal response.

III. RESULTS AND DISCUSSION

A. Spectral analysis

In Fig. 2, we show a spectrogram of the cell's response to pumping on the $F = 4 \rightarrow F' = 4$ transition. Video 1 also shows the time evolution of the cell's response for all four pumping arrangements. The electro-optic comb measures the cell transmittance on both the $F = 4 \rightarrow F' = 3$ and $F = 4 \rightarrow F' = 4$ transitions [see Fig. 1(b)]. We observe spectral modifications induced in both transitions when the pump is switched on at $t = 0$, which then rapidly disappear when the pump is switched off at $t = 250$ μs. Here, 40 repetitions of the pumping sequence are measured in real time and are averaged to improve the SNR. We show cross sections across Fig. 2 at some specific time steps on the left-hand side of Fig. 3. The experimental data are shown by the red dots, while a fit to the experimental data is given by the black solid curve. In the left-hand panels, the pump is detuned by approximately +13 MHz with respect to the center frequency of the $F = 4 \rightarrow F' = 4$ transition (as in Fig. 2), while the right side shows the pump at about +9 MHz with respect to the center of the $F = 3 \rightarrow F' = 3$ transition.

In each panel, we show the unperturbed resonance that is seen prior to the pump being switched on (the blue curve). This unperturbed resonance shows the standard Cs doublet: two Doppler-broadened absorption features with their
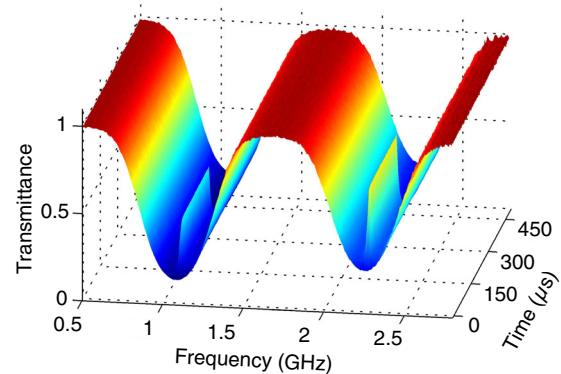

FIG. 2. Spectrogram showing the frequency-temporal response of the cesium $F = 4 \rightarrow F' = 3$, 4 transitions. A strong pump laser tuned to the $F = 4 \rightarrow F' = 4$ transition is switched on at $t = 0$ and switched off at $t = 250$ μs.

expected Voigt line shape [7]. The upper panels show the spectrum 2.2 μs after switching on the pump: on the left-hand side, we see a spectral hole arising from the pumping population from the $F = 4$ ground state into the $F = 3$ ground state. On the right-hand side, the pump transfers the population from the unobserved $F = 3$ ground state into the observed $F = 4$ ground state, and hence we see a narrow excess absorption feature (a spectral bump).

The middle panel shows the situation at $t = 168$ μs—the pumping feature is both deeper and broader than at the 2.2-μs point. Furthermore, by comparing the unperturbed resonance and the pumped spectra, we observe a broad pedestal of decreased absorption around the spectral hole, or a pedestal of excess absorption around the spectral bump. The lower panels show the transmission measured at $t = 260$ μs, 10 μs after the pump is switched off. The
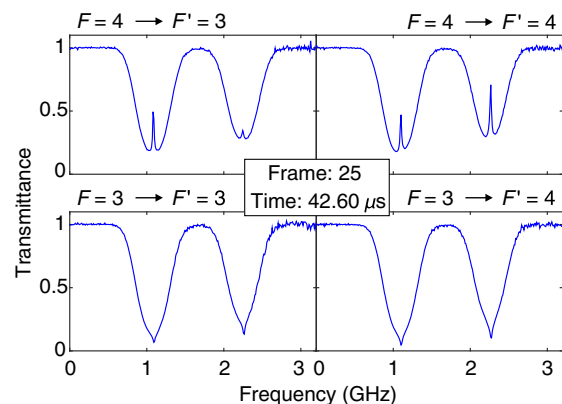
VIDEO 1. Time evolution of the transmittance measured on the cesium $F = 4 \rightarrow F' = 3$, 4 transitions for all four pumping scenarios around $t = 0$ and $t = 250$ μs. Some frames corresponding to a steady state between those two transition events are omitted to shorten the video.
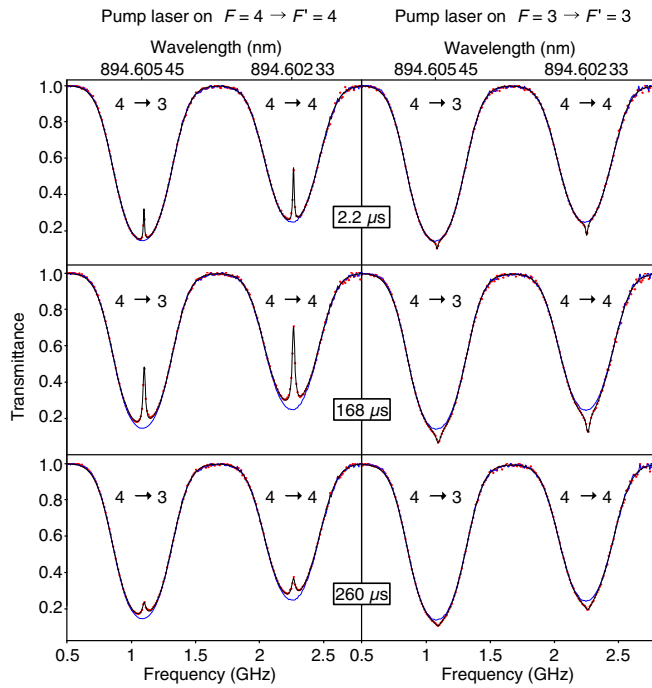
FIG. 3. Measured transmittance of the $F = 4 \rightarrow F' = 3, 4$ transitions. The left-hand column shows the outcome when pumping on the $F = 4 \rightarrow F' = 4$ transition, while the right-hand column displays pumping on the $F = 3 \rightarrow F' = 3$ transition. The top row shows 2.2 μs after the pump is switched on, the middle row shows the transmission at $t = 168$ μs, and the bottom row at $t = 260$ μs (10 μs after the pump is switched off). In each panel, we superimpose the unperturbed transmission spectrum (at $t = 0$, the blue line), together with a nonlinear fit to the experimental data (the black line). The wavelength markers are retrieved from Ref. [47].

narrow spectral feature has decreased rapidly in size by this time, while the amplitude of the pedestal decreases more slowly. For times beyond 268 μs, we see only the pedestal, and by $t \sim 285$ μs, the spectrum returns to looking observationally identical to the initial $t = 0$ spectrum.

We make a nonlinear fit to every experimental transmission measurement taken every 2.2 μs: a complete description of the fitting algorithm is given in Sec. I of the Supplemental Material [48]. The simple Voigt profile is a sufficiently good model in the conditions of this experiment. At low pressure in the vapor cell (approximately 1 μTorr at 22.2 °C [47]), no speed-dependant corrections to the line shape [49–51] are necessary. Furthermore, other line-shape corrections associated with optical pumping [7,52] are negligible at the signal-to-noise ratio of this experiment. The parameters of the unperturbed Doppler-broadened lines (widths of the Lorentzian and Gaussian components, central frequencies, and amplitudes of the two transitions) come from the initial transmittance curves (the blue curves in Fig. 3) and yield results consistent with the known atomic parameters [47] and the Doppler width at the temperature of the cell (22.2 °C) [7] (see Table 1 in the

Supplemental Material [48]). All but one of the parameters relating to the Doppler-broadened resonances are then held fixed for the rest of the series of fits; the one free parameter is an overall frequency shift to allow for any slow frequency drifts in the probe laser.

The necessity to include a broad pedestal to explain the physics is emphasized by Fig. 4, in which we compare the quality of the fits with and without the pedestal. In the upper panel, we set the pedestal amplitude to zero and the residuals show significant deviation from the data near the center of the absorption peaks. The lower panel allows for both pedestals and spectral holes and shows fit residuals (in transmittance) with a standard deviation of 6×10^{-3}: this level is consistent with the broadband noise of the detection process [40]. The pedestal is modeled with a Gaussian spectrum (see Sec. III D for details) with a fixed $1/e$ half-width of 80 MHz. The spectral width is experimentally determined by examining the temporal scans after 265 μs, where the pedestal is the dominant perturbation of the transmission.

At each temporal snapshot after switching on the pump, we fit the perturbed spectral curves with a function that allows for a spectral hole (or bump) that is treated as a Lorentzian function of arbitrary width, amplitude, and frequency along with a Gaussian-shaped pedestal function of arbitrary amplitude. The amplitude in both cases has
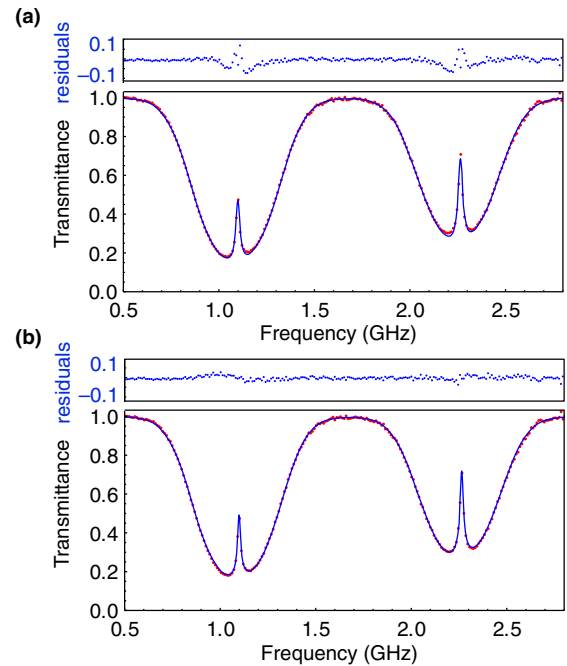

FIG. 4. Inclusion of a broad pedestal. (a) Fit using spectral holes only. The absence of the pedestal forces the widths of the resonant features to around 36 MHz. (b) Fit allowing for both spectral holes and pedestals. The returned width values for the resonant features are around 27 MHz. The displayed residuals are expressed in terms of the optical-depth difference between the model and fitted curves.

been expressed in terms of a fractional modification of the optical depth of the unperturbed resonance.

B. Temporal evolution

Figure 5 summarizes the evolution of the optical-pumping characteristics when the optical pump is tuned to the $F = 4 \rightarrow F' = 4$ transition (lower panel, corresponding to the left-hand side of Fig. 3), or the $F = 3 \rightarrow F' = 3$ transition (upper panel, corresponding to the right-hand side of Fig. 3). We obtain two independent estimates for the amplitude and the linewidth of the burnt features in each of the two transitions monitored by the comb [blue (red) for the $F = 4 \rightarrow F' = 4(3)$ transition]. The amplitude of the features nearly reaches its steady-state value within 2 μs. By contrast, the initial variation of the bandwidth (the right-hand side of the plot) happens on a slower time scale with a characteristic time of about 4 μs. Following a period in which the parameters maintain a stable value, we switch off the optical pump and note a relaxation of the amplitude of the features, with a characteristic time scale of approximately 7 μs in both monitor transitions. The parameters of the broad pedestal [the brown (black) curve for that observed in the $F = 4 \rightarrow F' = 4(3)$ transitions] shows

TABLE I. Steady-state amplitude (fractional change in optical depth) and bandwidth of the burnt features under the four pumping arrangements.

Pump transition $F \rightarrow F'$	Fractional amplitude $4 \rightarrow 3$	Fractional amplitude $4 \rightarrow 4$	Bandwidth (MHz) $4 \rightarrow 3$	Bandwidth (MHz) $4 \rightarrow 4$
$4 \rightarrow 4$	0.58	0.72	26.9	27.9
$4 \rightarrow 3$	0.65	0.19	25.1	35.1
$3 \rightarrow 4$	−0.45	−0.50	30.8	31.9
$3 \rightarrow 3$	−0.31	−0.36	31.6	29.1

an exponential or power-law-like increase and decrease with time constants of 24–26 μs that contrast strongly with those observed for the burnt features (see Sec. III in the Supplemental Material [48]). The response to pumping on the $F = 3 \rightarrow F' = 3$ transition is similar to that seen when pumping on the $F = 4 \rightarrow F' = 4$ transition (albeit with the opposite sign of the amplitude of the perturbations). We note, however, that the amplitude of the narrow feature appears to show an overshoot and then a relaxation to its steady-state value.

The steady-state amplitude and bandwidths of the spectral holes and bumps are shown in Table I—we note that the observed bandwidths are heavily broadened when compared to the natural linewidth (4.55 MHz) because of the saturation related to the optical pumping. The table also lists the outcomes from the other two possible configurations of the pump ($F = 4 \rightarrow F' = 3$ and $F = 3 \rightarrow F' = 4$), which show a qualitatively similar behavior to the $F = 4 \rightarrow F' = 4$ and $F = 3 \rightarrow F' = 3$ transitions, respectively (see Fig. 1 in the Supplemental Material [48]).

Figure 6 shows an unexpected temporal evolution of the frequency splitting between the spectral holes in the two monitored transitions for two different pumping arrangements: pumping on the $F = 4 \rightarrow F' = 3$ and $F = 4 \rightarrow F' = 4$ transitions. We display these particular pumping arrangements, as the observed frequency shift has its largest magnitude, although we see similar effects on all of the
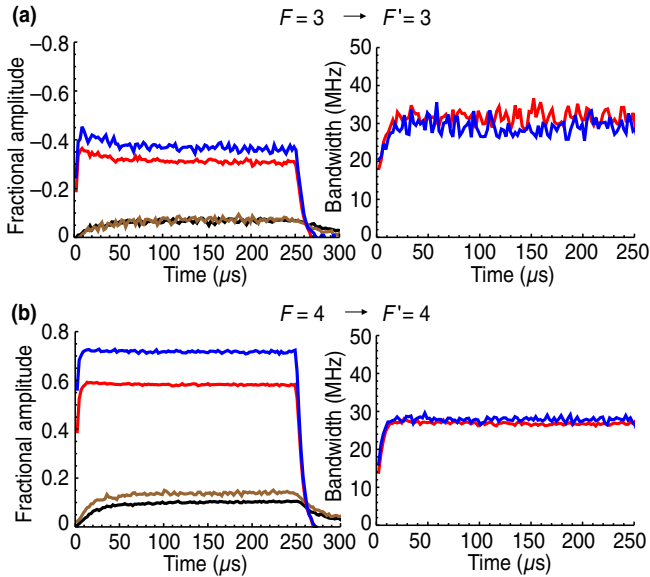

FIG. 5. Temporal evolution of the spectral modifications. (a) Pump tuned to the $F = 3 \rightarrow F' = 3$ transition. The left plot shows the fractional height (the fractional change in optical depth) of the spectral hole in the $F = 4 \rightarrow F' = 3$ (red) and $F = 4 \rightarrow F' = 4$ (blue) transitions. The amplitude of the pedestal feature is also shown as measured in the $F = 4 \rightarrow F' = 4$ (brown) and $F = 4 \rightarrow F' = 3$ (black) transitions. The right-hand-side plot shows the bandwidth of the burnt feature as measured in the $F = 4 \rightarrow F' = 3$ (red) and $F = 4 \rightarrow F' = 4$ (blue) transitions. (b) Pump tuned to the $F = 4 \rightarrow F' = 4$ transition. Color codes are the same as in (a). See Fig. 1 in the Supplemental Material [48] for the cases where the pump is tuned to the $F = 3 \rightarrow F' = 4$ and $F = 4 \rightarrow F' = 3$ transitions.
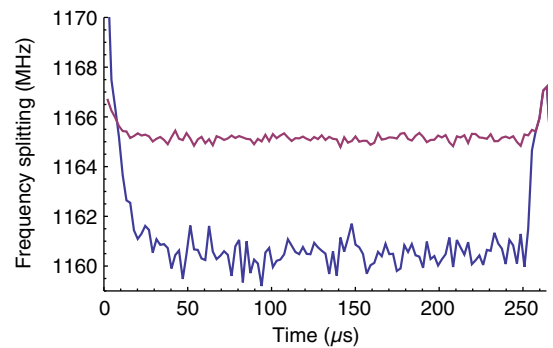

FIG. 6. Frequency splitting between spectral holes as a function of time when pumped on the $F = 4 \rightarrow F' = 3$ (blue) and $F = 4 \rightarrow F' = 4$ (red) transitions.

tested arrangements. The magnitude of these frequency shifts is in proportion to the difference in the coupling strength between each of the two monitor transitions and the pump field—in all cases, we see a reduction in the frequency splitting as a function of time. It is possible that the origin of this evolving splitting is a light shift (the ac Stark shift) due to a change in the effective pump intensity as a function of time. As the atomic transition saturates, the pump light penetrates further into the cell and thereby increases the average intensity in the cell. For all four pumping scenarios, we find an initial (before saturation sets in) frequency separation between the spectral holes of 1167.3 ± 0.1 MHz, which is in reasonable agreement with the known value of 1167.68 ± 0.08 MHz [47]. The small difference between those values could also be explained with light shifts associated with the pump, probe, or LO beams.

C. Theoretical model

We model the temporal evolution of the optical pumping effects on the atoms by transforming the four-level Cs atom into a simpler three-level system—two levels represent the ground states, $|g_{1,2}\rangle$, and the third level represents the excited state $|e\rangle$ (see Sec. II in the Supplemental Material [48]). When pumping from the $F = 3$ ground state, the pumping process cannot create strong polarization in the Zeeman states of the ground state, so a simple three-level model is sufficient to explain the observations. Our theoretical model allows for decay from the excited state to both ground-state levels, with a branching ratio, β, a decay rate from the excited state of Γ, and an on-resonance pumping rate, $2I\sigma/(h\nu)$, where I is the intensity of the laser and σ is the optical cross section of the transition [53]. We include a simple exponential relaxation process in each atomic level to allow for the transit of atoms through the optical-probe beam.

The output of an example calculation is shown in Fig. 7. Two parameters have been adjusted in this figure to match the experimental conditions in Fig. 5: the relaxation time constant of the ground-state populations is set at 7.5 μs to match the observed amplitude decay when the pump is extinguished. We can independently estimate the average transit-time relaxation rates for our geometry by averaging over the Maxwell-Boltzmann distribution as it crosses the 1.1-mm-radius probe and pump beams: this estimation gives an expected transit-time relaxation of approximately 6 μs. This number is in reasonable accord with the experiment, with a slight difference perhaps being explained by the few-degree misalignment of the pump and probe beams. The effective pumping rate in the model is set to 7 MHz to produce a steady-state bandwidth that agrees with that observed in the real experiment (see Table I). The measured pump-beam intensity is twice the saturation intensity of the Cs $D1$ transition, which would indicate a pumping rate of 28 MHz $\sim \Gamma$, where Γ is the excited-state
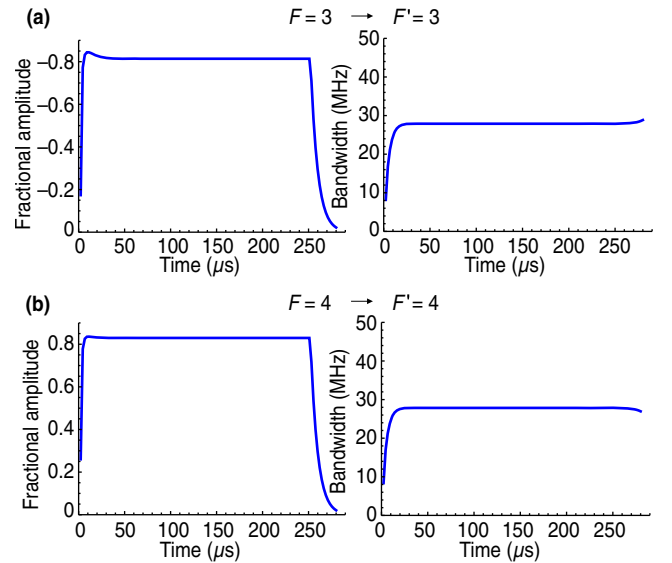

FIG. 7. Simulations of the atomic response using a three-level atomic model. (a) Pump tuned to the $F = 3 \rightarrow F' = 3$ transition. (b) Pump tuned to the $F = 4 \rightarrow F' = 4$ transition. In both cases, the pumping rate has been set at 7 MHz and transit-time relaxation at 7.5 μs. The theory shows good qualitative agreement with the experimental curves in Fig. 5.

relaxation rate. We believe that the effective pumping rate is significantly lowered because of the lack of overlap between the pump and probe beams because of their angular mismatch. We show the results for a wide range of different effective pumping rates in Sec. II of the Supplemental Material [48].

A comparison of Figs. 7 and 5 shows many qualitative features that are in good accord. The amplitude of the spectral modifications induced by the pump changes rapidly in the initial period at a rate proportional to the pumping rate. The approach to the steady state occurs on a time scale associated with the ground-state relaxation time, so, for very high intensities, we see an overshoot in the amplitude before a decrease back to the steady-state value. This effect is seen in both the experiment and the model. We also see an exponential increase in the bandwidth of the burnt feature as the population saturates—the model shows that the time scale of this process is set by both the intensity of the pump and the relaxation processes. For the parameters in Fig. 7, the model predicts an exponential time constant for the initial bandwidth change of 4.1 μs, which agrees with the observed value of 4 μs. The model shows that, at very low incident intensities, this time constant is equal to the transit-time relaxation time (7.5 μs), but at higher intensities, it is shortened: for a vapor driven at the saturation intensity, we see an approximate halving of this time constant.

The model also demonstrates that the steady-state amplitude of the observed spectral hole and bump depends on the pumping rate, which in turn depends on the intensity

of the pump laser and the optical cross section of the transition. In the experiment, the overlap between the pump and probe beams is not complete (an approximately 2° misalignment), which lowers the fractional population perturbation over that predicted by the model.

By reexamining Table I with the knowledge acquired from the model, we can now explain some of the variation seen there. The difference in the measured amplitude of the burnt features in the two absorption dips is within 14% when pumping out of the $F = 3$ ground state. This result reflects the case in which this pump arrangement produces a simple population perturbation in the ground state ($F = 4$) that leads to a common optical-depth variation in both observed transitions. By contrast, when the pump drives from the $F = 4$ ground state, we see an asymmetry in the apparent strength of the burnt features in the two resonances, as well as relatively larger amplitudes than when pumping from the $F = 3$ state; this effect is especially evident in the $F = 4 \rightarrow F' = 3$ pumping case. The asymmetry arises from optical pumping within the Zeeman levels of the ground state (ground-state polarization), which produces a dark state with an effectively higher transparency. Optical pumping is particularly strong in the $F = 4 \rightarrow F' = 3$ transition because the branching ratio from the upper state results in 3/4 of the atoms falling back into the $F = 4$ ground state, allowing for more pump-driven cycling. As expected, the dark state only appears when the probe and the pump are connected to the same transition—something that is evident when examining the asymmetry in the first two rows of Table I.

D. Pedestal

The pedestal dynamics are quite different from that seen in the spectral-hole and spectral-bump features. The pedestal increases in amplitude with a 26 ± 10 μs characteristic time, in stark contrast to the time for appearance of the narrow feature (approximately 2 μs). The pedestal also disappears more slowly than the narrow burnt feature, with an exponential time constant of 24 ± 4 μs across the various monitor transitions and pumping configurations, in comparison to the characteristic time for the decrease of the amplitude of the burnt features, which is around 7.5 μs. This behavior is consistent with a cross-relaxation process [54] arising from the reabsorption of radiation within the cell, which perturbs the thermal-equilibrium populations of the atoms outside the pump-beam volume. A naive estimate of the pedestal time scale is set by the time required for an atom to cross the vapor cell to enter the probe beam: this value is given by the cell radius, $r \sim 5$ mm, and the typical velocity, $v_0 = 192$ ms^{-1}, suggesting a pedestal time constant of $r/v_0 \sim 26$ μs, in agreement with the observed time. In Sec. III of the Supplemental Material [48], we present a more sophisticated model of radiation trapping in an optically deep, effusive vapor, which predicts fast and slow time scales in the optical response to a switched pump

beam. Previous models of radiation trapping have assumed either a static atomic vapor or a diffusive model for atomic motion [55]. Here, based on a 1D phenomenological model, we predict a slow time scale of around 20 μs, which is reasonably consistent with the observed time scale. The model also predicts a power-law decay of the pedestal response, as opposed to an exponential decay. We show that the experimental evolution is statistically consistent with a (modified) power law.

The spectral signature of such a reabsorption process has not been deeply considered in the literature, perhaps because it could not be easily observed. For the general case, one would expect it to have a spectral signature that is close to the Doppler width [54], although we observe a much narrower distribution than that. Consider resolving the velocity of some excited atom within the pump beam into two directions: along the beam (longitudinal) and transverse to the pump. The ensemble of excited atoms will have a narrow range of longitudinal velocities determined by the pump-beam frequency; however, spontaneous deexcitation can occur in any direction, leading to a distribution of Doppler shifts in the emitted photons associated with the unknown transverse velocity of the excited atoms. If we consider the direction defined by the vector joining the emitting atom and the reabsorption event, then a reabsorption will occur only if the absorbing atom has a velocity component along this vector that nearly matches that of the emitting atom. However, these reabsorbing atoms will again have a distribution of velocities in the plane transverse to this vector. Some fraction of these reabsorbing atoms, who now have modified ground-state populations due to this secondary absorption, will recross the probe beam and be observed in our transmission measurement. The spectral width of the perturbation in the probe beam will reflect the velocity spread of these reabsorbing atoms, as projected along the beam direction.

For an infinitely large cell, these processes lead to a Gaussian spectral signature with a width of the same order as the Doppler broadening. However, for a finite cell, the optical depth in an arbitrary direction may not be sufficient to give a high probability of reabsorption. In our cell, at room temperature, only a narrow cone of reemission angles ($\theta \sim 15°–20°$) around the pump direction will have a high probability of reabsorption. These atoms show a reduced velocity spread of the order of $\sqrt{2}\sin(\theta)v_{MB}$ when projected into the probe-beam direction, where v_{MB} is the most probable velocity in the Maxwell-Boltzmann distribution. This prediction is in reasonable agreement with the spectral width found experimentally (80 MHz vs the 214 MHz associated with the full Maxwell-Boltzmann distribution at this temperature).

IV. CONCLUSION

The acquisition of spectral data with both high frequency and high time resolution offers new insight into dynamical

processes. We make use of an electro-optic frequency-comb technology to open a new window into nature. We demonstrate an ability to make continuous observations of several atomic transitions in cesium with microsecond resolution. We perturb these lines with an auxiliary laser source and observe a number of physical effects that are unexpected. This set of effects includes temporal evolution of the bandwidth and frequency splitting of burnt features, as well as the influence of radiation reabsorption on the spectrum. We show that many of these effects can be explained using a dynamical model. Our findings on the effects of radiation reabsorption, which are made distinguishable from other competing effects by the time-resolved nature of the experiment, introduce corrections to spectroscopic models involving burnt spectral features.

ACKNOWLEDGMENTS

[1] C. S. Wood, S. C. Bennett, D. Cho, B. P. Masterson, J. L. Roberts, C. E. Tanner, and C. E. Wieman, Measurement of parity nonconservation and an anapole moment in cesium, Science **275**, 1759 (1997).

[2] P. Jönsson, A. Ynnerman, C. Froese Fischer, M. R. Godefroid, and J. Olsen, Large-scale multiconfiguration Hartree-Fock and configuration-interaction calculations of the transition probability and hyperfine structures in the sodium resonance transition, Phys. Rev. A **53**, 4021 (1996).

[3] T. Brage, C. F. Fischer, and P. Jönsson, Effects of core-valence and core-core correlation on the line strength of the resonance lines in Li I and Na I, Phys. Rev. A **49**, 2181 (1994).

[4] R. Hanson, Applications of quantitative laser sensors to kinetics, propulsion and practical energy systems, Proc. Combust. Inst. **33**, 1 (2011).

[5] P. Amodio, M. D. De Vizia, L. Moretti, and L. Gianfrani, Investigating the ultimate accuracy of doppler-broadening thermometry by means of a global fitting procedure, Phys. Rev. A **92**, 032506 (2015).

[6] A. Cygan, D. Lisak, S. Wójtewicz, J. Domyslawska, J. T. Hodges, R. S. Trawiński, and R. Ciurylo, High-signal-to-noise-ratio laser technique for accurate measurements of spectral line parameters, Phys. Rev. A **85**, 022508 (2012).

[7] G.-W. Truong, J. D. Anstie, E. F. May, T. M. Stace, and A. N. Luiten, Accurate lineshape spectroscopy and the Boltzmann constant, Nat. Commun. **6** (2015).

[8] T. M. Stace, Quantum limits of thermometry, Phys. Rev. A **82**, 011611 (2010).

[9] O. L. Polyansky, K. Bielska, M. Ghysels, L. Lodi, N. F. Zobov, J. T. Hodges, and J. Tennyson, High-Accuracy CO_2 Line Intensities Determined from Theory and Experiment, Phys. Rev. Lett. **114**, 243001 (2015).

[10] G. Larcher, X. Landsheere, M. Schwell, and H. Tran, Spectral shape parameters of pure CO_2 transitions near 1.6 μm by tunable diode laser spectroscopy, J. Quant. Spectrosc. Radiat. Transfer **164**, 82 (2015).

[11] C. E. Miller, L. R. Brown, R. A. Toth, D. C. Benner, and V. M. Devi, Spectroscopic challenges for high accuracy retrievals of atmospheric CO_2 and the Orbiting Carbon Observatory (OCO) experiment, C.R. Phys. **6**, 876 (2005).

[12] A. C. Ferrari and D. M. Basko, Raman spectroscopy as a versatile tool for studying the properties of graphene, Nat. Nanotechnol. **8**, 235 (2013).

[13] T. Ideguchi, S. Holzner, B. Bernhardt, G. Guelachvili, N. Picqué, and T. W. Hänsch, Coherent raman spectro-imaging with laser frequency combs, Nature (London) **502**, 355 (2013).

[14] R. Miller, The vibrational spectroscopy and dynamics of weakly bound neutral complexes, Science **240**, 447 (1988).

[15] M. S. Bradley and C. Bratu, Vibrational line profiles as a probe of molecular interactions, J. Chem. Educ. **74**, 553 (1997).

[16] J. A. Koch, R. E. Stewart, P. Beiersdorfer, R. Shepherd, M. B. Schneider, A. R. Miles, H. A. Scott, V. A. Smalyuk, and W. W. Hsing, High-resolution spectroscopy for Doppler-broadening ion temperature measurements of implosions at the National Ignition Facility, Rev. Sci. Instrum. **83**, 10E127 (2012).

[17] P. R. Griffiths, B. L. Hirsche, and C. J. Manning, Ultra-rapid-scanning Fourier transform infrared spectrometry, Vib. Spectrosc. **19**, 165 (1999).

[18] C. J. Manning, Smoke and mirrors: Ultra-rapid-scan FT-IR spectrometry, AIP Conf. Proc. **430**, 84 (1998).

[19] M. J. Thorpe, K. D. Moll, R. J. Jones, B. Safdi, and J. Ye, Broadband cavity ringdown spectroscopy for sensitive and rapid molecular detection, Science **311**, 1595 (2006).

[20] J. Dong, T. T.-Y. Lam, M. B. Gray, R. B. Warrington, E. H. Roberts, D. A. Shaddock, D. E. McClelland, and J. H. Chow, Optical cavity enhanced real-time absorption spectroscopy of CO_2 using laser amplitude modulation, Appl. Phys. Lett. **105**, 053505 (2014).

[21] M. Gorlicki, A. Peuriot, and M. Dumont, Study of velocity-changing collisions by time resolved saturated absorption, J. Phys. (Paris), Lett. **41**, 275 (1980).

[22] C. Lerminiaux and M. Dumont, Saturation-spectroscopy transients from Raman coherence between metastable levels, J. Opt. Soc. Am. B **3**, 477 (1986).

[23] P. Del'Haye, O. Arcizet, M. L. Gorodetsky, R. Holzwarth, and T. J. Kippenberg, Frequency comb assisted diode laser spectroscopy for measurement of microcavity dispersion, Nat. Photonics **3**, 529 (2009).

[24] K. Knabe, P. A. Williams, F. R. Giorgetta, M. B. Radunsky, C. M. Armacost, S. Crivello, and N. R. Newbury, Absolute

spectroscopy of N_2O near 4.5 μm with a comb-calibrated, frequency-swept quantum cascade laser spectrometer, Opt. Express **21,** 1020 (2013).

[25] M. C. Phillips, M. S. Taubman, B. E. Bernacki, B. D. Cannon, R. D. Stahl, J. T. Schiffern, and T. L. Myers, Real-time trace gas sensing of fluorocarbons using a swept-wavelength external cavity quantum cascade laser, Analyst **139,** 2047 (2014).

[26] I. Coddington, F. R. Giorgetta, E. Baumann, W. C. Swann, and N. R. Newbury, Characterizing fast arbitrary cw wave-forms with 1500 THz/s instantaneous chirps, IEEE J. Sel. Top. Quantum Electron. **18,** 228 (2012).

[27] Z. K. loannidis, P. M. Radmore, and I. P. Giles, Dynamic response of an all-fiber ring resonator, Opt. Lett. **13,** 422 (1988).

[28] M. C. Stowe, M. J. Thorpe, A. Pe'er, J. Ye, J. E. Stalnaker, V. Gerginov, and S. A. Diddams, Direct frequency comb spectroscopy, Adv. At. Mol. Opt. Phys. **55,** 1 (2008).

[29] A. Cingöz, D. C. Yost, T. K. Allison, A. Ruehl, M. E. Fermann, I. Hartl, and J. Ye, Direct frequency comb spectroscopy in the extreme ultraviolet, Nature (London) **482,** 68 (2012).

[30] S. A. Diddams, L. Hollberg, and V. Mbele, Molecular fingerprinting with the resolved modes of a femtosecond laser frequency comb, Nature (London) **445,** 627 (2007).

[31] L. Nugent-Glandorf, F. R. Giorgetta, and S. A. Diddams, Open-air, broad-bandwidth trace gas sensing with a mid-infrared optical frequency comb, Appl. Phys. B **119,** 327 (2015).

[32] A. J. Fleisher, B. J. Bjork, T. Q. Bui, K. C. Cossel, M. Okumura, and J. Ye, Mid-infrared time-resolved frequency comb spectroscopy of transient free radicals, J. Phys. Chem. Lett. **5,** 2241 (2014).

[33] A. Zolot, F. Giorgetta, E. Baumann, J. Nicholson, W. Swann, I. Coddington, and N. Newbury, Direct-comb molecular spectroscopy with accurate, resolved comb teeth over 43 THz, Opt. Lett. **37,** 638 (2012).

[34] J. Roy, J.-D. Deschênes, S. Potvin, and J. Genest, Continu-ous real-time correction and averaging for frequency comb interferometry, Opt. Express **20,** 21932 (2012).

[35] F. Keilmann, C. Gohle, and R. Holzwarth, Time-domain mid-infrared frequency-comb spectrometer, Opt. Lett. **29,** 1542 (2004).

[36] A. Schliesser, M. Brehm, F. Keilmann, and D. van der Weide, Frequency-comb infrared spectrometer for rapid, remote chemical sensing, Opt. Express **13,** 9029 (2005).

[37] T. Ideguchi, B. Bernhardt, G. Guelachvili, T. W. Hänsch, and N. Picqué, Raman-induced Kerr-effect dual-comb spectroscopy, Opt. Lett. **37,** 4498 (2012).

[38] F. Zhu, T. Mohamed, J. Strohaber, A. A. Kolomenskii, T. Udem, and H. A. Schuessler, Real-time dual frequency comb spectroscopy in the near infrared, Appl. Phys. Lett. **102,** 121116 (2013).

[39] I. Coddington, W. C. Swann, and N. R. Newbury, Coherent Multiheterodyne Spectroscopy Using Stabilized Optical Frequency Combs, Phys. Rev. Lett. **100,** 013902 (2008).

[40] N. B. Hébert, V. Michaud-Belleau, J. D. Anstie, J.-D. Deschênes, A. N. Luiten, and J. Genest, Self-heterodyne interference spectroscopy using a comb generated by pseudo-random modulation, Opt. Express **23,** 27806 (2015).

[41] T. Sakamoto, T. Kawanishi, and M. Izutsu, Widely wavelength-tunable ultra-flat frequency comb generation using conventional dual-drive Mach-Zehnder modulator, Electron. Lett. **43,** 1 (2007).

[42] D. Long, A. Fleisher, K. Douglass, S. Maxwell, K. Bielska, J. Hodges, and D. Plusquellic, Multiheterodyne spectro-scopy with optical frequency combs generated from a continuous-wave laser, Opt. Lett. **39,** 2688 (2014).

[43] V. Durán, S. Tainta, and V. Torres-Company, Ultrafast electrooptic dual-comb interferometry, Opt. Express **23,** 30557 (2015).

[44] G. Millot, S. Pitois, M. Yan, T. Hovhannisyan, A. Bendahmane, T. W. Hänsch, and N. Picqué, Frequency-agile dual-comb spectroscopy, Nat. Photonics **10,** 27 (2016).

[45] Y. Bao, X. Yi, Z. Li, Q. Chen, J. Li, X. Fan, and X. Zhang, A digitally generated ultrafine optical frequency comb for spectral measurements with 0.01-pm resolution and 0.7-μs response time, Light Sci. Appl. **4,** e300 (2015).

[46] J. Reichert, R. Holzwarth, T. Udem, and T. W. Hänsch, Measuring the frequency of light with mode-locked lasers, Opt. Commun. **172,** 59 (1999).

[47] D. A. Steck, http://steck.us/alkalidata (2010).

[48] See Supplemental Material at http://link.aps.org/supplemental/10.1103/PhysRevApplied.6.044012 for de-tails on the fitting algorithm and on the dynamical model and for a 1D model of radiation trapping in an effusive vapor.

[49] M. Triki, C. Lemarchand, B. Darquié, P. L. T. Sow, V. Roncin, C. Chardonnet, and C. Daussy, Speed-dependent effects in NH3 self-broadened spectra: Towards the deter-mination of the Boltzmann constant, Phys. Rev. A **85,** 062510 (2012).

[50] R. Ciurylo, R. Jaworski, J. Jurkowski, A. S. Pine, and J. Szudy, Spectral line shapes modeled by a quadratic speed-dependent galatry profile, Phys. Rev. A **63,** 032507 (2001).

[51] L. Gianfrani, Highly-accurate line shape studies in the near-IR spectrum of H_2 ^{18}O: Implications for the spectroscopic determination of the Boltzmann constant, J. Phys. Conf. Ser. **397,** 012029 (2012).

[52] T. M. Stace, G.-W. Truong, J. Anstie, E. F. May, and A. N. Luiten, Power-dependent line-shape corrections for quanti-tative spectroscopy, Phys. Rev. A **86,** 012506 (2012).

[53] D. A. Steck, http://steck.us/teaching (2011).

[54] A. E. Siegman, *Lasers* (University Science Books, South Orange, NJ, 1986).

[55] A. F. Molisch, B. P. Oehry, W. Schupita, and G. Magerl, Radiation trapping in atomic vapours in finite-cylinder vapour cells excited by a laser beam, J. Phys. B **30,** 1879 (1997).